

# The effect of Cu oxidation states on C<sub>2</sub>H<sub>4</sub> production from electrochemical CO<sub>2</sub> conversion

Gaeun Park<sup>a,1</sup>, Hyunki Kim<sup>a,1</sup>, Gyeong Ho Han<sup>a</sup>, Juho Ha<sup>a</sup>, Jung Yong Seo<sup>b</sup>, Minji Kang<sup>b</sup>, Myung-gi Seo<sup>b</sup>, Younghoon Choi<sup>b</sup>, Soo Young Kim<sup>c,\*</sup>, Sang Hyun Ahn<sup>a,\*</sup>

<sup>a</sup> School of Chemical Engineering and Material Science, Chung-Ang University, Seoul 06974, Republic of Korea

<sup>b</sup> Lotte Chemical Institute of Technology, Daejeon 34110, Republic of Korea

<sup>c</sup> Department of Materials Science and Engineering, Korea University, Seoul 02841, Republic of Korea

## ARTICLE INFO

### Keywords:

Electrochemical CO<sub>2</sub> reduction  
Cu-based catalysts  
Oxidized Cu species  
C<sub>2</sub>H<sub>4</sub> production  
Zero-gap electrolyzer

## ABSTRACT

Recently, many studies have reported on the significant role of Cu<sup>δ+</sup>/Cu<sup>0</sup> in the production of C<sub>2</sub>H<sub>4</sub>, highlighting the enhanced activity of oxidized Cu electrodes compared to metallic Cu electrodes. However, there is relatively little research that compares catalytic performance for C<sub>2</sub>H<sub>4</sub> production in membrane electrode assembly (MEA)-type cells. Herein, we present an analysis of the performance of Cu-based oxidized cathodes in MEA-type cells, specifically focusing on the Cu oxidation state in relation to the CO<sub>2</sub> reduction reaction (CO<sub>2</sub>RR). Both metallic Cu and oxidized Cu cathodes were prepared via a simple electroless deposition and subsequent oxidation process. The electric, chemical, and thermal oxidation methods yielded Cu electrodes with distinct electronic structures. Subsequently, the CO<sub>2</sub>RR performance of these electrodes was evaluated in single MEA-type cells, and the correlation between the Cu<sup>0-1+</sup> ratio and their performance was studied. Our findings confirmed that the ability to form C<sub>2</sub>H<sub>4</sub> follows a volcano-shaped trend based on the Cu<sup>0-1+</sup> ratio. Furthermore, a stability test was conducted for CO<sub>2</sub>RR at a cell voltage of 3.2 V, revealing that the initially highly active Cu-based cathode exhibited notably poor stability in the MEA-type cell test.

## 1. Introduction

Greenhouse gases have been identified as a significant contributor to global warming, with CO<sub>2</sub> making up over 80% of these greenhouse gases [1,2]. Various strategies have been explored to address the challenges associated with CO<sub>2</sub> emissions, including carbon capture and carbon utilization (e.g., biochemical, photochemical, and electrochemical) [3–6]. The electrochemical CO<sub>2</sub> reduction reaction (CO<sub>2</sub>RR) method offers distinct advantages by enabling the production of high-value chemicals while simultaneously mitigating carbon dioxide emissions via integration with renewable energy sources. Techno-economic evaluations of CO<sub>2</sub>RR indicate that to achieve a positive net present value, a selectivity exceeding 80% and an energy efficiency of 50% are essential [7]. In conventional H-type cell systems, aqueous CO<sub>2</sub> solutions are used as reactants, which limitations on the maximum current density of the product due to the low solubility of CO<sub>2</sub>. Recently, advanced CO<sub>2</sub> electrolysis systems have been developed, including the gaseous CO<sub>2</sub>-fed flow cell and the catholyte-free

membrane electrode assembly (MEA)-based electrolyzer. The CO<sub>2</sub>-fed flow cell uses a catholyte chamber positioned between the cathode and membrane, allowing for the straightforward detection of both gaseous and liquid products. Nonetheless, the presence of the catholyte can adversely impact the cathode environment and introduce significantly high ohmic resistance during the CO<sub>2</sub>RR. In contrast, MEA-type electrolyzers adopt a zero-gap configuration between the anode and cathode, thereby minimizing ohmic resistance. Additionally, MEA-type electrolyzers offer facile scalability and cell stacking, unlike flow-type cells [8].

Focusing on the range of carbon chemicals that can be generated via the CO<sub>2</sub>RR process, C<sub>2</sub>H<sub>4</sub> stands out as an appealing product due to its higher energy density compared to other C<sub>1</sub> chemicals, as well as its high commercial value due to a large market demand [9]. It is widely acknowledged that the formation of C<sub>2</sub>H<sub>4</sub> is primarily limited by the C–C coupling step, which can occur through three distinct cases: \*CO–\*CO, \*CO–\*COH, or \*CO–\*CHO [10]. Among single metal catalysts, Cu stands out as the only catalyst capable of producing C<sub>2</sub>H<sub>4</sub> products such as C<sub>2</sub>H<sub>4</sub>

\* Corresponding authors.

E-mail addresses: [sooyoungkim@korea.ac.kr](mailto:sooyoungkim@korea.ac.kr) (S.Y. Kim), [shahn@cau.ac.kr](mailto:shahn@cau.ac.kr) (S.H. Ahn).

<sup>1</sup> These authors contributed equally to this work.

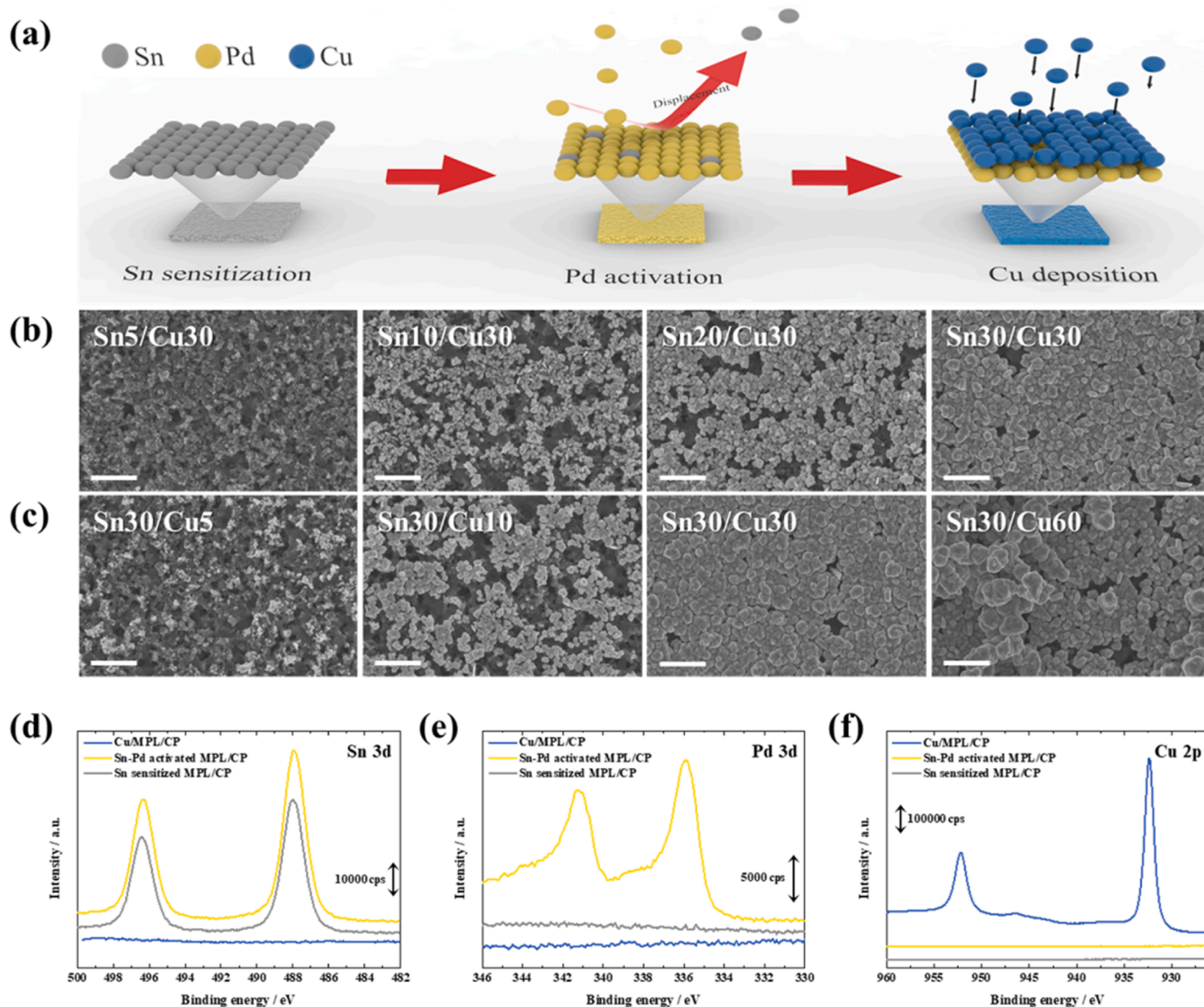


**Fig. 1.** (a) Schematic illustration of Cu ELD on MPL/CP. FESEM images of the Cu deposits prepared by varying (b) Sn sensitization time, and (c) Cu ELD time. The scale bar represents 1  $\mu\text{m}$ . The XPS spectra of Cu/MPL/CP, Sn-Pd activated MPL/CP, and Sn sensitized MPL/CP for (d) Sn 3d, (e) Pd 3d, and (f) Cu 2p.

and C<sub>2</sub>H<sub>5</sub>OH [11]. The adsorption energy of the intermediate \*CO on the copper surface is neither excessively weak nor excessively strong, thereby facilitating C–C coupling to produce C<sub>2</sub>H<sub>4</sub> [12]. However, the high energy barrier associated with C–C coupling results in poor C<sub>2</sub>H<sub>4</sub> selectivity for Cu catalysts, presenting a significant challenge in the development of high-performance Cu electrodes specifically tailored for C<sub>2</sub>H<sub>4</sub> production. Numerous studies have focused on accelerating C–C coupling by adjusting the various properties of Cu electrode such as morphology [13,14], facets [15,16], and electronic structure [17,18].

Among them, Cu-based oxide or compound catalysts have exhibited higher Faradaic efficiency (FE) for C<sub>2</sub>H<sub>4</sub> production, with their superior performance attributed to the presence of Cu <sup>$\delta$ +</sup> ( $0 < \delta \leq 1$ ) species. The active site responsible for this performance has been a subject of debate, but theoretical calculations have indicated that the coexistence of Cu <sup>$\delta$ +</sup> and Cu<sup>0</sup> species can improve the kinetics and thermodynamics of CO<sub>2</sub> activation [19] and reduce the energy barrier for \*CO dimerization [19–23]. In addition, recently reported review paper discovered a correlation between the chemical state and selectivity by summarizing Cu<sup>+</sup>/Cu<sup>0</sup> atomic ratio in previously reported in situ/Operando studies on Cu catalysts. When the atomic ratio of Cu<sup>0</sup> species on the Cu surface

exceeds 20%, there is a significant shift in product selectivity from CO/HCOO<sup>–</sup> to C<sub>2</sub>H<sub>4</sub> or C<sub>2</sub>H<sub>5</sub>OH. Then the atomic ratio exceeds 95%, the priority shifts from C<sub>2</sub> products to the favorable production of CH<sub>4</sub> [24].

Remaining challenge associated with Cu catalyst containing Cu <sup>$\delta$ +</sup> species is their susceptibility to reduction to Cu<sup>0</sup> during CO<sub>2</sub>RR, leading to a degradation of C–C coupling [25,26]. Various strategies have been proposed to stabilize Cu <sup>$\delta$ +</sup> species on the catalyst surface, including heteroatom doping [27,28], ligand addition [29], support introduction [30], morphology engineering [31], and grain boundary manipulation [20]. Most studies on Cu <sup>$\delta$ +</sup> species have reported catalytic performance using H-type cells [22,27,30,32,33] or flow cell-type cells with a catholyte [20]. However, the evaluation of Cu electrodes based on their oxidation states in H-type cells or flow-type cells can be challenging due to the easy oxidation of metallic Cu catalysts into Cu(OH)<sub>2</sub> and CuO forms in alkaline electrolytes [22]. On the other hand, a recent study using Operando X-ray absorption spectroscopy to evaluate Cu electrodes in MEA-type cells demonstrated the stability of certain oxidized Cu species, such as Cu<sub>2</sub>O and Cu(OH)<sub>2</sub>, even under strong reducing conditions during the CO<sub>2</sub>RR [22]. Despite these findings, the application of Cu-based oxide or oxide-derived electrodes for C<sub>2</sub>H<sub>4</sub> production in the

cathode of MEA-type cells has been relatively limited [21,22].

In this study, the performance of Cu-based electrodes for CO<sub>2</sub>RR in MEA-based cells was investigated, with a particular focus on Cu valency. A simple electroless deposition (ELD) method was used to prepare a Cu layer on a gas diffusion layer, followed by subsequent chemical, thermal, and electrical oxidation processes to oxidize the Cu electrode. The relationship between the oxidized Cu ratio and the ability to produce C<sub>2</sub>H<sub>4</sub> was explored in the MEA-based cell setup.

## 2. Experimental setup

### 2.1. Characterization

The surface morphology of the prepared Cu-based catalysts was investigated through field-emission scanning electron microscopy (FESEM, Sigma, Carl Zeiss) and transmission electron microscopy (TEM, JEM-2100 F, JEOL Ltd.) analyses. To determine the crystal structure of the catalysts, X-ray diffraction (XRD, Bruker-AXS, New D8 Advance) and high-resolution TEM (HRTEM) analyses with fast Fourier transform (FFT) patterns were performed. Additionally, an X-ray photoelectron spectroscopy (XPS, K-alpha+, Thermo Fisher Scientific) analysis was conducted to determine the surface composition of the catalysts.

### 2.2. Preparation of Cu electrode by ELD method

The microporous layer coated-carbon paper (MPL/CP) was used as the substrate for the ELD process. The preparation of catalyst nuclei involved two steps: Sn sensitization and subsequent Pd activation on MPL/CP. Sn sensitization was carried out for 30 min using a solution composed of 0.59 g SnCl<sub>2</sub>, 6 mL HCl, and 100 mL deionized water. Following Sn sensitization, the MPL/CP substrate was immersed in a Pd activation solution containing 0.02 g PdCl<sub>2</sub>, 0.6 mL HCl, and 200 mL deionized water for 20 s. The substrate was then rinsed in deionized water for 10 s to remove any residual solution. After the Sn–Pd treatment, Cu ELD was performed on the activated substrate for 30 min using a solution containing 4 mM CuSO<sub>4</sub>·5H<sub>2</sub>O, 8 mM ethylenediaminetetraacetic acid, 70 mM para-formaldehyde, and 69 mM KOH. The ELD process was conducted at a constant deposition temperature of 60 °C,

maintained using a thermostat.

### 2.3. Oxidation of Cu/MPL/CP

The copper catalysts (Cu/MPL/CP) prepared in this study were subjected to oxidation using electrical, chemical, and thermal methods. For electrical oxidation, a three-electrode half-cell connected to a potentiostat was used. Cu/MPL/CP was used as the working electrode, a graphite rod was used as the counter electrode, and Hg/HgO (1 M NaOH) was used as the reference electrode. A constant potential of –0.05 or 0.05 V<sub>Hg/HgO</sub> was applied in a 0.1 M KOH solution for 10 min. The chemical oxidation method involved immersing the pristine Cu/MPL/CP in a solution containing 2.5 M NaOH and 0.125 M (NH<sub>4</sub>)<sub>2</sub>S<sub>2</sub>O<sub>8</sub> at room temperature for varying from 1 to 40 min. The thermal oxidation was carried out via an annealing process using a furnace in an air atmosphere at 180, 280, or 380 °C for 3 h.

### 2.4. CO<sub>2</sub>RR performance measurement in MEA-type cells

To assess the catalytic performance of the prepared electrodes, an anion exchange membrane (AEM)-based MEA-type CO<sub>2</sub> electrolytic cell was used. The Cu-based electrodes prepared in this study were used as the cathode, while a commercial IrO<sub>2</sub>/CP (C0206, Dioxide Materials) electrode was used as the anode. A membrane (AEM: Sustainion X37–50, Dioxide Materials) was positioned between the cathode and anode. Gaskets with a thickness of 200 μm were used for both the anode and cathode sides. The active area of the single cell was 1.0 cm<sup>2</sup>, and the electrolyzer was assembled with a torque of 60 lb-in. Humidified CO<sub>2</sub> gas was supplied to the back side of the cathode at a flow rate of 200 mL/min, while 20 mL/min of 0.1 M KOH was supplied to the anode side. The CO<sub>2</sub>RR performance was evaluated by applying a constant potential for 15 min at room temperature. The outlet of each electrolyzer was connected to a gas chromatograph (GC, Agilent 7890B) equipped with a thermal conductivity detector (TCD) and a flame ionization detector to determine the concentrations of gaseous products (H<sub>2</sub>, CO, CH<sub>4</sub>, and C<sub>2</sub>H<sub>4</sub>). The concentrations and charges of each product were used to calculate the FE and partial current density (PCD).

## 3. Results and discussion

### 3.1. Fabrication and characterization of metallic Cu electrode

Cu/MPL/CP was synthesized using a simple ELD method on MPL/CP substrates (Fig. 1). Prior to Cu ELD, the Sn–Pd activation process was carried out on MPL/CP, as shown in Fig. 1a. This two-step activation procedure involving Sn sensitization and subsequent Pd displacement is used as a convenient pretreatment method for Cu ELD on hydrophobic substrates, due to the strong adsorption capability of Sn<sup>2+</sup> species [34–36].

To achieve a uniform Cu layer on MPL/CP, the conditions for Sn sensitization and Cu ELD were adjusted, while the Pd galvanic displacement condition remained constant throughout the experiments. Initially, the Sn sensitization time was varied from 5 to 30 min, while the Cu ELD time was fixed at 30 min (Fig. 1b shows the FESEM images of the Cu deposits obtained at different Sn sensitization times (Sn#/Cu30, #: Sn sensitization time). In the case of Sn5/Cu, some nanoparticles smaller than 50 nm were observed, but the MPL/CP surface remained largely exposed due to the low coverage of Cu deposits. As the Sn sensitization time increased, the size of the Cu particles gradually increased, resulting in increased Cu coverage. When the Sn sensitization time was increased to 30 min, the MPL/CP surface was completely covered by Cu particles measuring 100–200 nm. Therefore, the Sn sensitization time was fixed at 30 min, and the Cu ELD time was varied from 5 to 60 min. The morphology of the Cu deposits (Sn30/Cu#, #: Cu ELD time) was examined via FESEM analysis. When the Cu ELD time was less than 30 min, poor coverage of Cu deposits was observed. On the other hand,

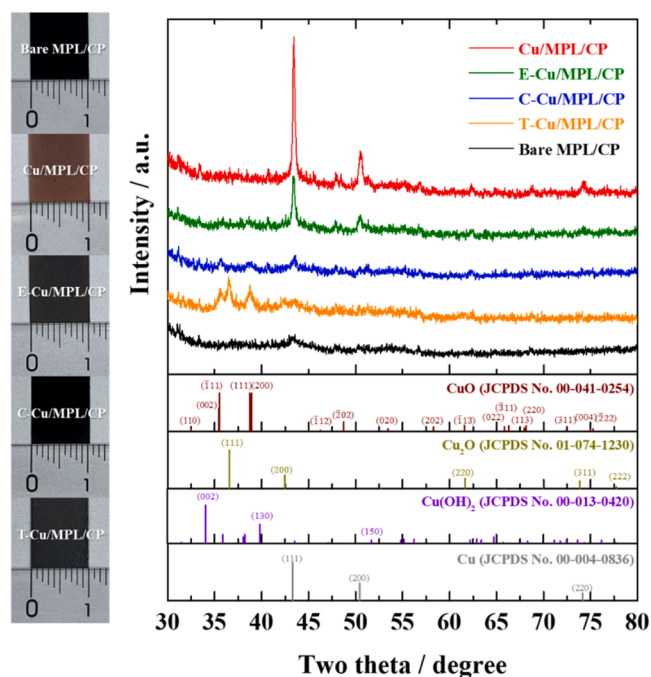
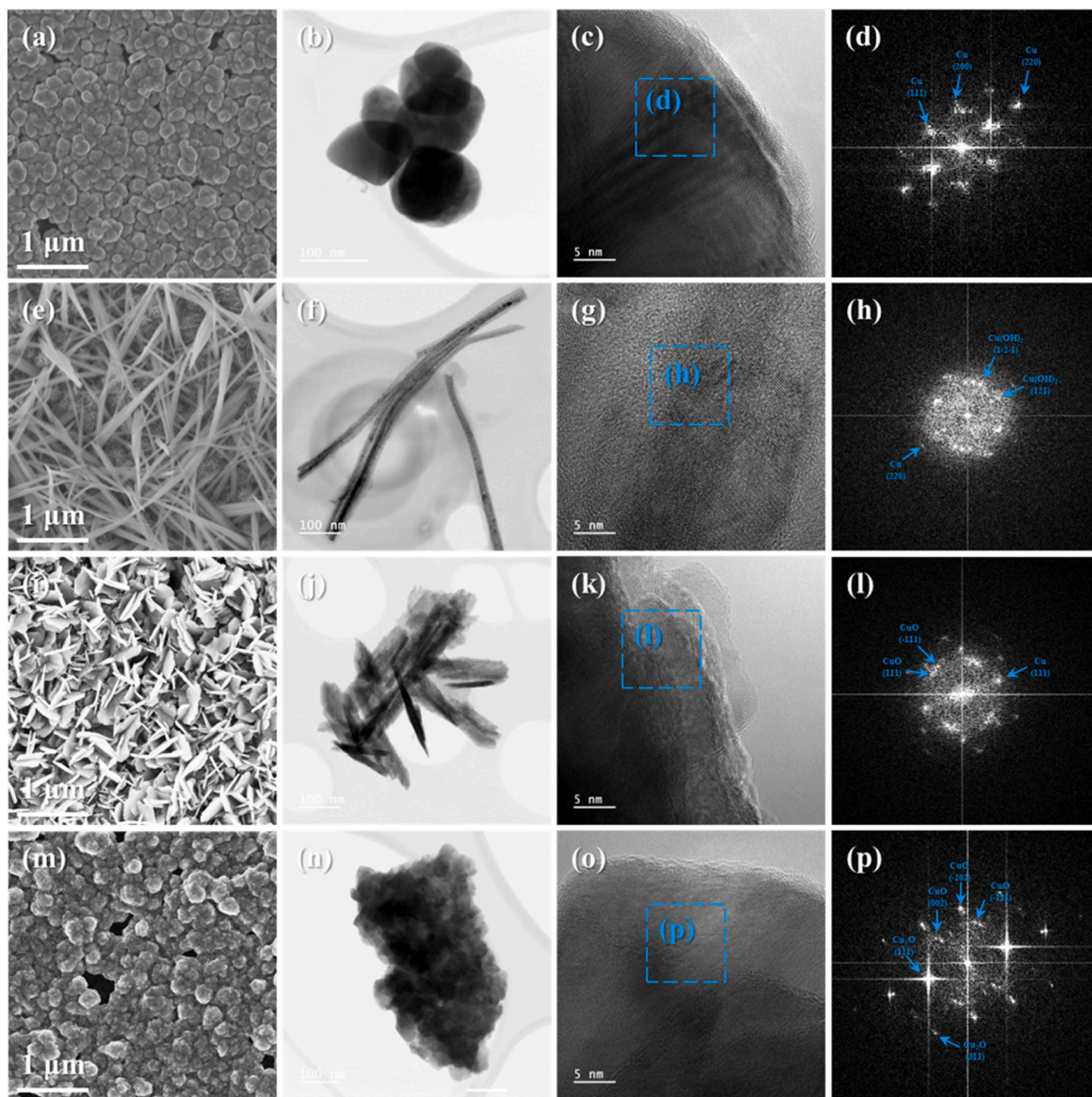


Fig. 2. Images and XRD analysis results of the bare MPL/CP, Cu/MPL/CP, E-Cu/MPL/CP, C-Cu/MPL/CP, and T-Cu/MPL/CP.



**Fig. 3.** FESEM, TEM, HRTEM images, and FFT patterns corresponding to the marked area for (a–d) Cu/MPL/CP, (e–h) E-Cu/MPL/CP, (i–l) C-Cu/MPL/CP, and (m–p) T-Cu/MPL/CP.

when the Cu ELD time exceeded 30 min (Sn30/Cu60), aggregation of Cu deposits was observed. Based on the FESEM results, both Sn sensitization and Cu ELD times were fixed at 30 min, resulting in the optimized sample denoted as Cu/MPL/CP. Notably, it is difficult to distinguish the morphology of Sn-Pd-activated MPL/CP from bare MPL/CP (Fig. S1). However, the presence of the Cu deposit was observed after the Cu ELD process (Fig. 1b–c), indicating that the formation of Pd particles on MPL/CP serves as a nucleation site for Cu growth [34–36]. The XPS analysis further supports the presence of Sn (Fig. 1d) and Pd (Fig. 1e) on MPL/CP after Sn sensitization and the subsequent Pd activation step. After the Cu ELD process (Cu/MPL/CP), a sharp Cu 2p peak was observed, while the Sn and Pd spectra could not be discerned.

### 3.2. Fabrication and characterization of oxidized Cu electrode

The prepared Cu/MPL/CP electrode underwent oxidation via three methods: electrical, chemical, and thermal oxidation. Each oxidation condition, the resulting changes in morphology, and the CO<sub>2</sub>RR performance of the electrodes in the MEA-type cell were investigated (Figs. S2–4). The specific experimental conditions can be found in the Experiment setup section. The optimal condition for each oxidation method was determined based on the highest activity observed for C<sub>2</sub>H<sub>4</sub> production at 3.2 V<sub>cell</sub> (Figs. S2–4). The electrically oxidized Cu electrode was denoted as E-Cu/MPL/CP, the chemically oxidized Cu electrode was denoted as C-Cu/MPL/CP, and the thermally oxidized Cu electrode

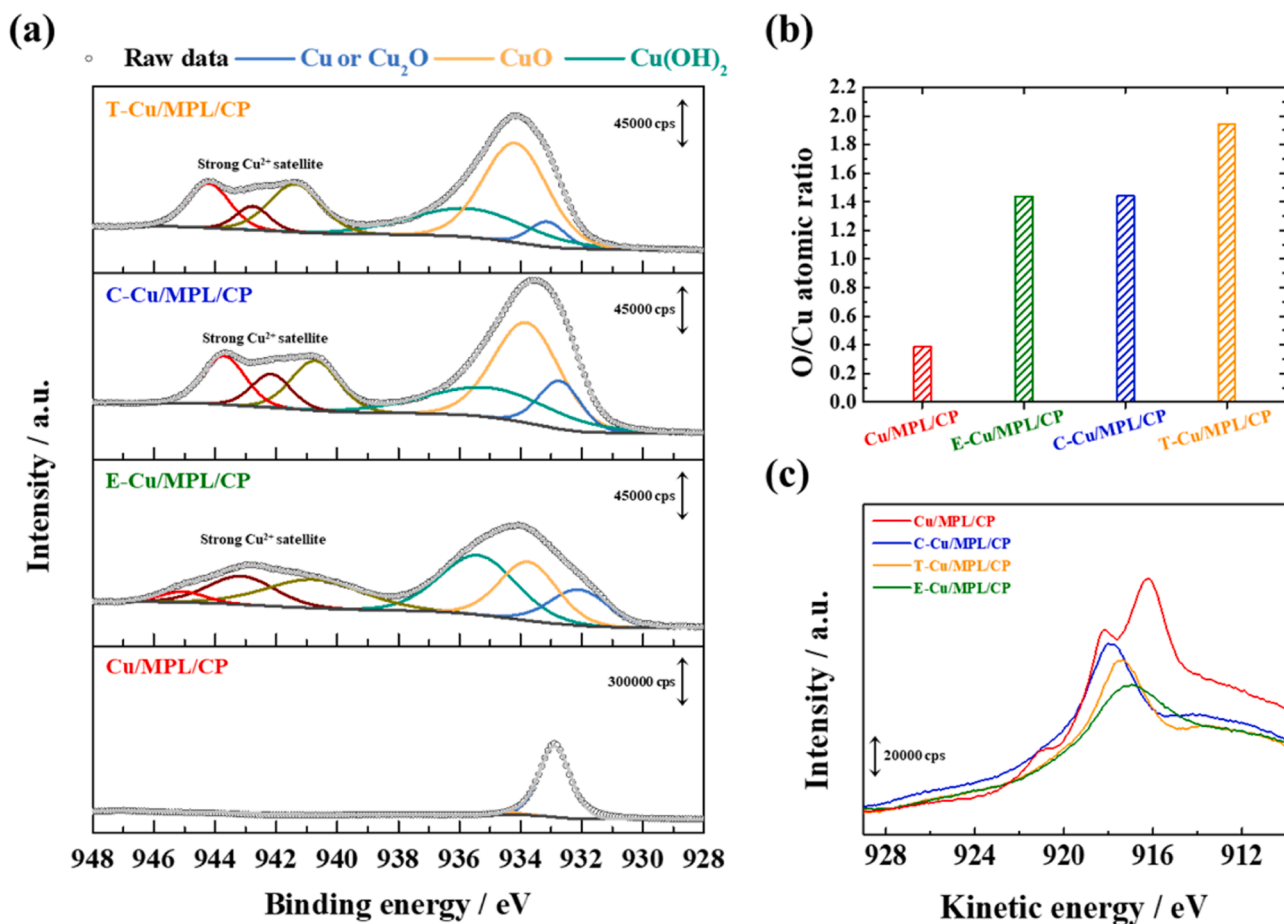


Fig. 4. (a) Deconvoluted Cu 2p<sub>3/2</sub> spectra of prepared electrodes, (b) summarization of O/Cu ratio for each electrode, and (c) Cu LMM Auger spectra of each electrode.

was denoted as T-Cu/MP/CP, reflecting the respective oxidation methods used.

The images of the prepared Cu-based electrode (Fig. 2) indicated that they exhibited different colors after the oxidation process, indicating the variations in their material properties, including oxidation state [37,38]. An XRD analysis was performed to further investigate the crystal structure of the Cu-based electrodes. The XRD patterns of Cu/MPL/CP revealed distinct diffraction peaks corresponding to metallic Cu. However, after the oxidation process, the intensity of the metallic Cu peak decreased. In the XRD pattern of E-Cu/MPL/CP, there were no discernible peaks corresponding to Cu(OH)<sub>2</sub>, Cu<sub>2</sub>O, or CuO. For C-Cu/MPL/CP, a small peak was observed at approximately 35.7° and 38.7°, corresponding to the (-111) and (111) planes of CuO, respectively. In the case of T-Cu/MPL/CP, distinct peaks corresponding to metallic Cu could not be observed, but sharp peaks corresponding to Cu<sub>2</sub>O and CuO peaks were detected.

Fig. 3 presents the results of the FESEM and TEM analysis. In both the FESEM (Fig. 3a) and TEM images (Fig. 3b), a consistent nanoparticle shape was observed for Cu/MPL/CP. However, after the electrical oxidation process (E-Cu/MPL/CP), the morphology transformed into a nanoneedle structure (Fig. 3e, f), which is similar to previously reported studies on Cu(OH)<sub>2</sub>-CuO nanoneedles catalysts for the methanol oxidation reaction [39,40]. For C-Cu/MPL/CP, a nanosheet morphology was observed (Fig. 3i, j). Generally, the chemical oxidation method is used to fabricate Cu(OH)<sub>2</sub> nanoneedles [41–43]. However, if the oxidation process is prolonged, Cu(OH)<sub>2</sub> nanoneedles can transform into CuO sheets [41]. This trend is clearly observed in Fig. S3 and is consistent with the XRD analysis. On the other hand, T-Cu/MPL/CP (Fig. 3m, n) exhibited a nanoparticle shape similar to that of

Cu/MPL/CP. The EDS mapping images of the oxidized electrode in Fig. S5 indicate a uniform distribution of Cu and O signals. Additionally, the crystallinity of each electrode was investigated using HRTEM with FFT patterns.

In all cases, the corresponding FFT patterns (Fig. 3d, h, l, p) revealed a polycrystalline structure with distinct diffraction patterns. Without oxidation, Cu/MPL/CP exhibited metallic Cu lattice planes corresponding to the (111), (200), and (220) facets. However, in the FFT patterns of E-Cu/MPL/CP and C-Cu/MPL/CP, it can be observed that some of the metallic Cu transformed into Cu(OH)<sub>2</sub> (Fig. 3h) or CuO (Fig. 3l), respectively. In the case of T-Cu/MPL/CP, the absence of metallic Cu lattice planes was noted, and the presence of crystal facets corresponding to Cu<sub>2</sub>O and CuO was confirmed (Fig. 3p).

An XPS analysis was conducted to analyze the surface composition of the electrodes, as shown in Figs. 4 and S6. Fig. 4a presents the deconvoluted Cu 2p<sub>3/2</sub> spectra of the electrodes [44,45]. In the case of Cu/MPL/CP, the presence of CuO and Cu(OH)<sub>2</sub> peaks was negligible, with the majority of the peaks being deconvoluted into a single large peak corresponding to Cu or Cu<sub>2</sub>O. However, for the oxidized electrodes, a significant increase in the ratio of CuO and Cu(OH)<sub>2</sub> peaks were observed, accompanied by a strong Cu<sup>2+</sup> satellite peak.

The XPS analysis revealed important insights into the surface composition of the electrodes. Specifically, among the oxidized electrodes, E-Cu/MPL/CP exhibited a significantly higher ratio of Cu(OH)<sub>2</sub> peaks, while C-Cu/MPL/CP and T-Cu/MPL/CP exhibited similar deconvoluted peak patterns. However, the peak corresponding to Cu or Cu<sub>2</sub>O was slightly lower in T-Cu/MPL/CP compared to C-Cu/MPL/CP. Fig. S6 presents the O 1s spectra of Cu/MPL/CP and oxidized Cu/MPL/CP. All Cu-based electrodes exhibited distinct O 1s spectra, though

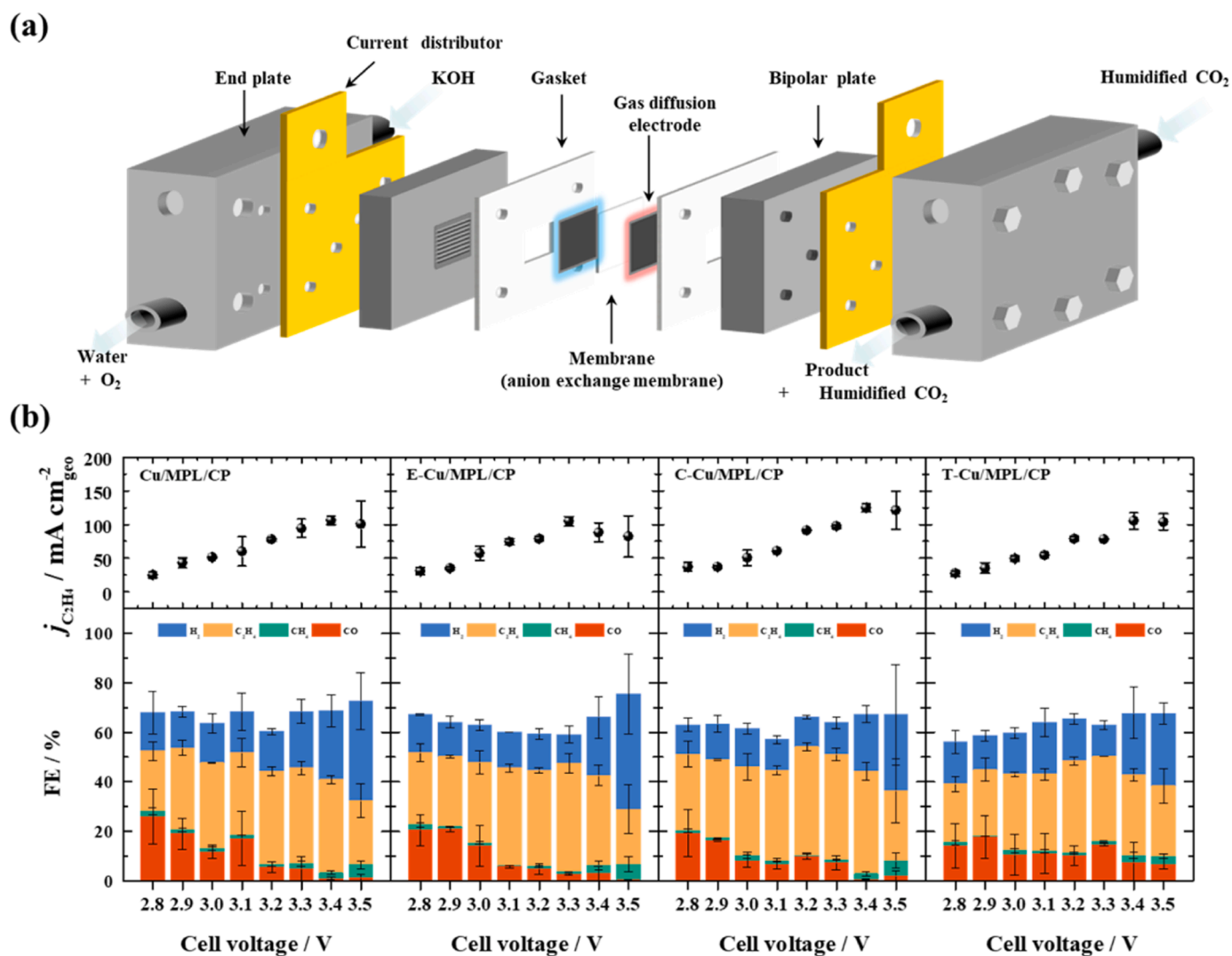


Fig. 5. (a) Schematic illustration of the MEA-type CO<sub>2</sub> electrolyzer, and (b) FE and PCD of C<sub>2</sub>H<sub>4</sub> as depending on applied cell voltage for Cu-based electrodes.

slight variations were observed. Notably, three peaks were observed in the approximate range of 532.0, 531.0, and 529.5–530.0 eV. The peaks around 531.0 and 532.0 eV have been commonly associated with absorbed water molecules, oxygen species, or hydroxyl groups, but the precise positioning of these peaks has been inconsistent [46–49]. On the other hand, the peak positioned at the lower binding energy range of 529.5–530.0 eV is widely accepted as a peak associated with lattice oxygen [46]. The presence of distinct peaks for lattice oxygen was clearly observed in the oxidized electrodes, which were not observed in the Cu/MPL/CP electrode. Based on the XPS results, the O/Cu ratio of each electrode was calculated and summarized in Fig. 4b. The highest O/Cu ratio was observed in T-Cu/MPL/CP, followed by C-Cu/MPL/CP, E-Cu/MPL/CP, and Cu/MPL/CP. Additionally, the Cu LMM Auger spectra of each electrode were examined in Fig. 4c. The Cu LMM spectra for Cu/MPL/CP displayed two Cu peaks at 918.1 eV and 917.7 eV corresponding to Cu<sup>0</sup> and Cu<sup>1+</sup>, respectively [29,50]. In contrast, the oxidized Cu electrodes exhibited a broad peak positioned at kinetic energy values of 916.9, 917.4, and 918.0 eV for E-Cu/MPL/CP, T-Cu/MPL/CP, and C-Cu/MPL/CP, respectively. Compared to previously reported kinetic energy of CuO powder (917.8 eV) [50], there are clear differences in peak position, indicating the coexistence of various oxidized Cu species.

### 3.3. CO<sub>2</sub>RR performance test of Cu-based cathode in MEA-type cell

The CO<sub>2</sub>RR performance of both Cu/MPL/CP and oxidized Cu electrodes was assessed in an MEA-type single cell, as depicted in Fig. 5a. To prevent the autoxidation of the Cu surface [48], the electrodes were promptly introduced into the MEA as cathodes immediately after fabrication for direct evaluation. The CO<sub>2</sub>RR performance of the single cell was measured via chronoamperometry for 15 min (Fig. S7), and the stabilized current density within the time range of 840–900 s was used to evaluate the catalytic performance of each cathode (shown in Fig. S8).

Total FE of the gas product and PCD of C<sub>2</sub>H<sub>4</sub> are summarized in Fig. 5b. Notably, the total FE only reached approximately 60–80% in all CO<sub>2</sub>RR performance tests, indicating that the current density could contribute to the formation of other liquid products such as formic acid, ethanol, or propanol. Upon assuming that the remaining 40% of FE corresponds to 100% conversion of formic acid, ethanol, and propanol individually, the calculated volumes for all products were found to be below 1 mL, indicating that the liquid product analysis was challenging due to their very small quantities. Therefore, this study focused solely on the analysis and evaluation of gas products. A consistent trend was observed in all cathodes. As the cell voltage increased from 2.8 to 3.3 V<sub>cell</sub>, the FE of CO gradually decreased while the FE of C<sub>2</sub>H<sub>4</sub> increased. Furthermore, within the cell voltage range of 2.8–3.5 V, the FE of CH<sub>4</sub> was strongly suppressed to below 11%. These findings suggest

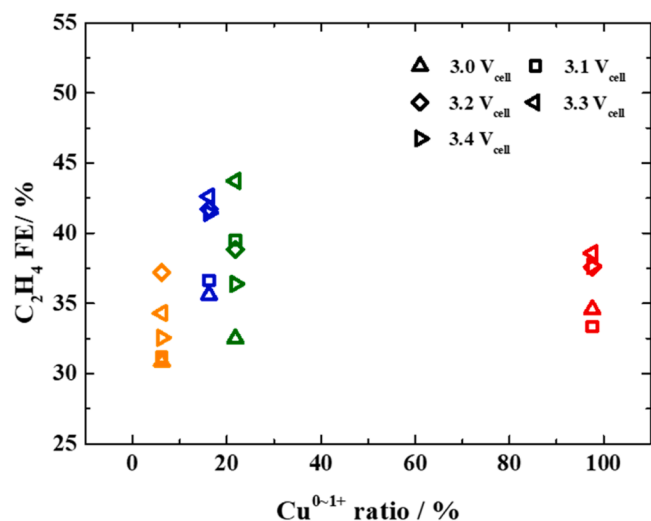


Fig. 6. C<sub>2</sub>H<sub>4</sub> FE of CO<sub>2</sub> electrolyzer with a Cu-based cathode as a function of Cu<sup>0-1+</sup> in the cell voltage range of 3.0–3.4 V<sub>cell</sub>.

that Cu-based cathodes favorably facilitate C-C coupling, thereby promoting the formation of C<sub>2</sub>H<sub>4</sub> over CH<sub>4</sub>. Upon reaching the peak C<sub>2</sub>H<sub>4</sub> FE at 3.2–3.4 V<sub>cell</sub>, a decline in C<sub>2</sub>H<sub>4</sub> FE was observed, which can be attributed to the pronounced occurrence of the hydrogen evolution reaction. Notably, the E-Cu/MPL/CP exhibited the highest C<sub>2</sub>H<sub>4</sub> FE of 47.7% at 3.3 V<sub>cell</sub>. To compare the mass activity of Cu-based cathodes, the Cu loading amounts were calculated using a combination of the weighing method and bulk composition obtained by EDS results. For T-Cu/MPL/CP, the loading amount was assumed to be the same as that of Cu/MPL/CP due to the mild oxidation conditions considered. The loading amount of Cu/MPL/CP was 0.286 mg/cm<sup>2</sup>, while E-Cu/MPL/CP and C-Cu/MPL/CP, which underwent oxidation processes, exhibited slightly lower values of 0.228 mg/cm<sup>2</sup> and 0.203 mg/cm<sup>2</sup>, respectively (Fig. S9a). This decrease in Cu loading is attributed to the partial dissolution of Cu(OH)<sub>2</sub> [51,52]. Based on the measured Cu loading, mass activity and turn over frequency (TOF) for C<sub>2</sub>H<sub>4</sub> of each cathode were calculated [53,54]. The mass normalized-PCD at 3.2 V<sub>cell</sub> summarized in Fig. S9b. The C-Cu/MPL/CP demonstrates the highest mass activity, reaching 480.8 mA mg<sup>-1</sup>. Following this, E-Cu/MPL/CP shows a slightly lower value, while Cu/MPL/CP and T-Cu/MPL/CP exhibit slightly lower values that are nevertheless comparable to each other. This trend is also evident in Fig. S10, which compares TOF of each Cu-based cathode.

Furthermore, considering the coexistence of Cu<sup>δ+</sup> and Cu<sup>0</sup>, which promote C-C coupling reactions, the C<sub>2</sub>H<sub>4</sub> formation activity was examined by comparing the Cu<sup>0-1+</sup> ratio in each cathode. The C<sub>2</sub>H<sub>4</sub> FE of each electrode was determined within the cell voltage range of 3.0–3.4 V, where a high selectivity towards C<sub>2</sub>H<sub>4</sub> was observed. Fig. 6 illustrates the correlation between the C<sub>2</sub>H<sub>4</sub> FE and the Cu<sup>0-1+</sup> ratio, which was calculated based on the XPS results. While some variation was observed depending on the cell voltage, the overall trend of the C<sub>2</sub>H<sub>4</sub> FE displayed a characteristic volcano-shaped pattern in relation to the Cu<sup>0-1+</sup> ratio. The C<sub>2</sub>H<sub>4</sub> FE increased with an increasing Cu<sup>0-1+</sup> ratio, reaching a maximum value of 21.8%, after which it started to decrease. This finding is in contrast with previously reported *in situ* studies on oxygen-containing Cu, which emphasized the crucial role of Cu<sup>δ+</sup> species in C<sub>2</sub>H<sub>4</sub> production. This discrepancy can be attributed to the rapid reduction of highly oxidized Cu species during the CO<sub>2</sub>RR test. Recent studies employing Operando X-ray absorption spectroscopy analysis to evaluate Cu electrodes in MEA-type cells demonstrated that the Cu<sup>2+</sup> species generated at a reverse cell voltage of 3.0 V underwent rapid reduction. Nonetheless, some oxidized species remained, with the majority reverting to Cu<sup>0</sup> species [22]. These findings provide supporting evidence for the observed volcano relationship depicted in Fig. 6.

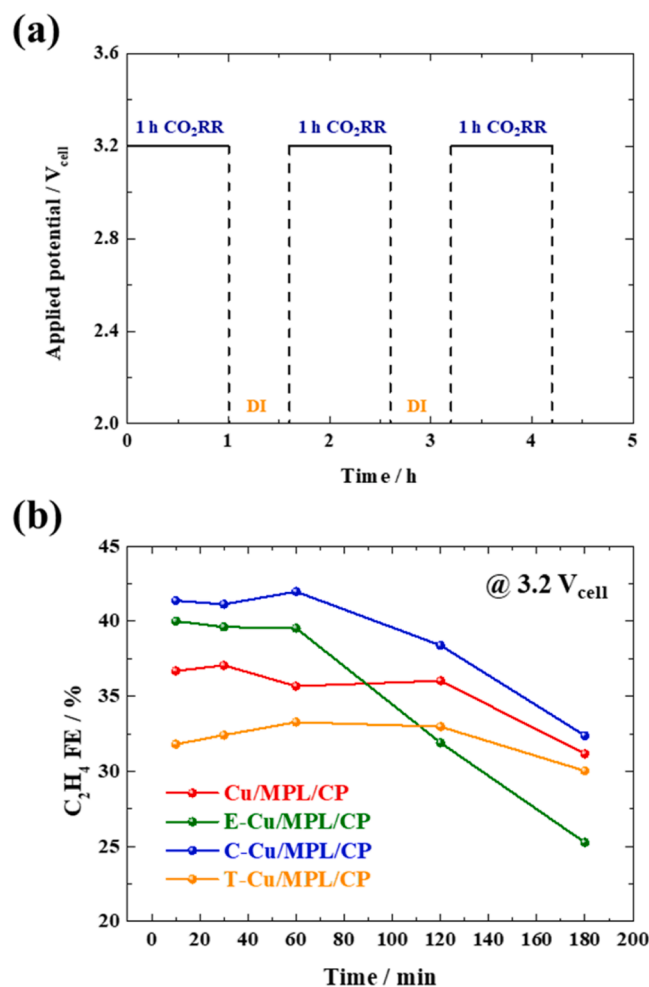


Fig. 7. (a) Schematic diagram of stability test for the CO<sub>2</sub>RR, and (b) C<sub>2</sub>H<sub>4</sub> FE of CO<sub>2</sub> electrolyzer with a Cu-based cathode as a function of CO<sub>2</sub> electrolysis time.

Furthermore, a stability test was conducted by applying a cell voltage of 3.2 V over 3 h (Figs. 7a and S11). The gas products were analyzed at 10, 30, 60, 120, and 180 min, as shown in Fig. S12. During the test, a 5 mL/min flow of deionized water was passed through the cathode side of the MEA for 3 min every hour. The cathode was subsequently dried using CO<sub>2</sub> gas at a flow rate of 200 mL/min before resuming the stability test. The presence of deionized water was crucial to prevent the formation of carbonate salt, which could lead to the blockage of the cathode channel before the completion of the stability test [21,55].

Fig. 7b presents a plot of C<sub>2</sub>H<sub>4</sub> FE as a function of CO<sub>2</sub>RR operation time. Interestingly, the stability of the Cu-based electrodes exhibited an inverse relationship to their initial activity, with T-Cu/MPL/CP exhibiting the highest stability followed by Cu/MPL/CP, C-Cu/MPL/CP, and E-Cu/MPL/CP. The C<sub>2</sub>H<sub>4</sub> FE was well-maintained for the first hour but subsequently experienced a rapid decrease. Notably, E-Cu/MPL/CP exhibited a significant decrease in C<sub>2</sub>H<sub>4</sub> FE, while the FE for CH<sub>4</sub> increased after 1 h. These findings suggest a diminished capability for C-C coupling due to the rapid reduction of Cu<sup>δ+</sup> species to Cu<sup>0</sup> during the CO<sub>2</sub>RR test. On the other hand, Cu/MPL/CP, which contains a higher proportion of metallic Cu species (Fig. 4), is expected to be less affected by this strong reducing environment. Investigating the stability of Cu<sup>δ+</sup> species following the CO<sub>2</sub>RR test in MEA-type cells remains a challenge. Future studies should explore cutting-edge *in situ* techniques to study the Cu electronic structure and monitor the Cu valency of the catalyst surface during the CO<sub>2</sub>RR test in MEA-type cells.

## 4. Conclusion

Cu electrodes were prepared on MPL/CP substrates using a simple ELD method, and subsequent electrical, chemical, and thermal oxidation steps enabled precise control of the oxidation state of Cu/MPL/CP. XRD and XPS analyses confirmed the coexistence of various Cu species in Cu/MPL/CP and the oxidized electrodes. Notably, all Cu-based cathodes exhibited C<sub>2</sub>H<sub>4</sub> production exceeding 35%. The E-Cu/MPL/CP electrode achieved the highest C<sub>2</sub>H<sub>4</sub> FE of 47.7% at a cell voltage of 3.3 V<sub>cell</sub>. Furthermore, the correlation between the Cu<sup>0-1+</sup> ratio and C<sub>2</sub>H<sub>4</sub> FE was investigated based on the XPS results, revealing a volcano-shaped relationship. The C<sub>2</sub>H<sub>4</sub> FE reached a maximum when the Cu<sup>0-1+</sup> ratio reached 21.8%, followed by a gradual decrease. However, during the stability test at a cell voltage of 3.2 V, the C<sub>2</sub>H<sub>4</sub> FE exhibited a decreasing trend according to the initial activity order. These findings highlight the significant influence of the Cu oxidation state on the initial activity and stability of the CO<sub>2</sub>RR operation in MEA-type cells.

## CRedit authorship contribution statement

**Gaeun Park:** Methodology, Visualization, Investigation. **Hyunki Kim:** Visualization, Investigation, Writing. **Juho Ha:** Investigation, **Jung Yong Seo:** Investigation. **Minji Kang:** Investigation. **Myung-gi Seo:** Investigation. **Youngeon Choi:** Conceptualization, Funding acquisition. **Soo Young Kim:** Conceptualization, Funding acquisition. **Sang Hyun Ahn:** Conceptualization, Methodology, Writing, Supervision. **Gyeong Ho Han:** Investigation.

## Declaration of Competing Interest

The authors declare that they have no known competing financial interests or personal relationships that could have appeared to influence the work reported in this paper.

## Data availability

Data will be made available on request.

## Acknowledgments

This research was supported by the National Research Foundation of Korea (NRF) grant funded by the Korea government MSIT (2021R1A2C2093358, 2021R1A4A3027878). This research was supported by the H2KOREA funded by the Ministry of Education (2022Hydrogen fuel cell-003, Innovative Human Resources Development Project for Hydrogen Fuel Cells). Authors also appreciate financial support from Lotte Chemical Company.

## Appendix A. Supporting information

Supplementary data associated with this article can be found in the online version at [doi:10.1016/j.jcou.2023.102569](https://doi.org/10.1016/j.jcou.2023.102569).

## References

- [1] K. Xiang, F. Shen, Y. Fu, L. Wu, Z. Wang, H. Yi, X. Liu, P. Wang, M. Liu, Z. Lin, H. Liu, Boosting CO<sub>2</sub> electroreduction towards C<sub>2+</sub> products via CO\* intermediate manipulation on copper-based catalysts, *Environ. Sci. Nano* 9 (2022) 911–953, <https://doi.org/10.1039/D1EN00977J>.
- [2] R.M. Arán-Ais, F. Scholten, S. Kunze, R. Rizo, Roldan B. Cuenya, The role of in situ generated morphological motifs and Cu (i) species in C<sub>2+</sub> product selectivity during CO<sub>2</sub> pulsed electroreduction, *Nat. Energy* 5 (2020) 317–325, <https://doi.org/10.1038/s41560-020-0594-9>.
- [3] E. Barton Cole, P.S. Lakkaraju, D.M. Rampulla, A.J. Morris, E. Abelev, A. B. Bocarsly, Using a one-electron shuttle for the multielectron reduction of CO<sub>2</sub> to methanol: kinetic, mechanistic, and structural insights, *J. Am. Chem. Soc.* 132 (2010) 11539–11551, <https://doi.org/10.1021/ja1023496>.
- [4] E.E. Benson, C.P. Kubiak, A.J. Sathrum, J.M. Smieja, Electrocatalytic and homogeneous approaches to conversion of CO<sub>2</sub> to liquid fuels, *Chem. Soc. Rev.* 38 (2009) 89–99, <https://doi.org/10.1039/B804323J>.
- [5] C.D. Windle, R.N. Perutz, Advances in molecular photocatalytic and electrocatalytic CO<sub>2</sub> reduction, *Coord. Chem. Rev.* 256 (2012) 2562–2570, <https://doi.org/10.1016/j.ccr.2012.03.010>.
- [6] J. Schneider, H. Jia, J.T. Muckerman, E. Fujita, Thermodynamics and kinetics of CO<sub>2</sub>, CO, and H<sup>+</sup> binding to the metal centre of CO<sub>2</sub> reduction catalysts, *Chem. Soc. Rev.* 41 (6) (2012) 2036–2051, <https://doi.org/10.1039/C1CS15278E>.
- [7] H. Shin, K.U. Hansen, F. Jiao, Techno-economic assessment of low-temperature carbon dioxide electrolysis, *Nat. Sustain.* 4 (10) (2021) 911–919, <https://doi.org/10.1038/s41893-021-00739-x>.
- [8] W.H. Lee, K. Kim, C. Lim, Y.-J. Ko, Y.-J. Hwang, B.K. Min, U. Lee, H.-S. Oh, New strategies for economically feasible CO<sub>2</sub> electroreduction using a porous membrane in zero-gap configuration, *J. Mater. Chem. A* 9 (2021) 16169–16177, <https://doi.org/10.1039/D1TA03182A>.
- [9] P. De Luna, C. Hahn, D. Higgins, S.A. Jaffer, T.F. Jaramillo, E.H. Sargent, What would it take for renewably powered electrosynthesis to displace petrochemical processes? *Science* 364 (2019) eaav3506, <https://doi.org/10.1126/science.aav3506>.
- [10] G.H. Han, J. Bang, G. Park, S. Choe, Y.J. Jang, H.W. Jang, S.Y. Kim, S.H. Ahn, Recent advances in electrochemical, photochemical, and photoelectrochemical reduction of CO<sub>2</sub> to C<sub>2+</sub> products, *Small* (2023), 2205765, <https://doi.org/10.1002/smll.202205765>.
- [11] Y. Wang, H. Shen, K.J.T. Livi, D. Raciti, H. Zong, J. Gregg, M. Onadeko, Y. Wan, A. Watson, C. Wang, Copper nanocubes for CO<sub>2</sub> reduction in gas diffusion electrodes, *Nano Lett.* 19 (2019) 8461–8468, <https://doi.org/10.1021/acs.nanolett.9b02748>.
- [12] Y. Wang, J. Liu, G. Zheng, Designing copper-based catalysts for efficient carbon dioxide electroreduction, *Adv. Mater.* 33 (2021), 2005798, <https://doi.org/10.1002/adma.202005798>.
- [13] J.J. Lv, M. Jouny, W. Luc, W. Zhu, J.J. Zhu, F. Jiao, A highly porous copper electrocatalyst for carbon dioxide reduction, *Adv. Mater.* 30 (2018), 1803111, <https://doi.org/10.1002/adma.201803111>.
- [14] M.G. Kibria, C.T. Dinh, A. Seifitokaldani, P. De Luna, T. Burdyny, R. Quintero-Bermudez, M.B. Ross, O.S. Bushuyev, F.P. Garcia de Arquer, P. Yang, D. Sinton, E. H. Sargent, A surface reconstruction route to high productivity and selectivity in CO<sub>2</sub> electroreduction toward C<sub>2+</sub> hydrocarbons, *Adv. Mater.* 30 (2018), 1804867, <https://doi.org/10.1002/adma.201804867>.
- [15] C. Choi, S. Kwon, T. Cheng, M. Xu, P. Tieu, C. Lee, J. Cai, H.M. Lee, X. Pan, X. Duan, W.A. Goddard, Y. Huang, Highly active and stable stepped Cu surface for enhanced electrochemical CO<sub>2</sub> reduction to C<sub>2</sub>H<sub>4</sub>, *Nat. Catal.* 3 (2020) 804–812, <https://doi.org/10.1038/s41929-020-00504-x>.
- [16] L. Zaza, K. Rossi, R. Buonsanti, Well-defined copper-based nanocatalysts for selective electrochemical reduction of CO<sub>2</sub> to C<sub>2</sub> products, *ACS Energy Lett.* 7 (2022) 1284–1291.
- [17] N. Hongrutai, S. Watmanee, P. Pinthong, J. Panpranot, Electrochemical reduction of carbon dioxide on the oxide-containing electrocatalysts, *J. CO<sub>2</sub> Util.* 64 (2022), 102194, <https://doi.org/10.1016/j.jcou.2022.102194>.
- [18] X. Ren, X. Zhang, X. Cao, Q. Wang, Efficient electrochemical reduction of carbon dioxide into ethylene boosted by copper vacancies on stepped cuprous oxide, *J. CO<sub>2</sub> Util.* 38 (2020) 125–131, <https://doi.org/10.1016/j.jcou.2020.01.018>.
- [19] H. Xiao, W.A. Goddard III, T. Cheng, Y. Liu, Cu metal embedded in oxidized matrix catalyst to promote CO<sub>2</sub> activation and CO dimerization for electrochemical reduction of CO<sub>2</sub>, *Proc. Natl. Acad. Sci.* 114 (2017) 6685–6688, <https://doi.org/10.1073/pnas.1702405114>.
- [20] X. Lv, Q. Liu, J. Wang, X. Wu, X. Li, Y. Yang, J. Yan, A. Wu, H.B. Wu, Grain refining enables mixed Cu<sup>+</sup>/Cu<sup>0</sup> states for CO<sub>2</sub> electroreduction to C<sub>2+</sub> products at high current density, *Appl. Catal. B Environ.* 324 (2023), 122272, <https://doi.org/10.1016/j.apcatb.2022.122272>.
- [21] N.H. Tran, H.P. Duong, G. Rousse, S. Zanna, M.W. Schreiber, M. Fontecave, Selective ethylene production from CO<sub>2</sub> and CO reduction via engineering membrane electrode assembly with porous dendritic copper oxide, *ACS Appl. Mater. Interfaces* 14 (2022) 31933–31941, <https://doi.org/10.1021/acsami.2c06068>.
- [22] W.H. Lee, C. Lim, S.Y. Lee, K.H. Chae, C.H. Choi, U. Lee, B.K. Min, Y.J. Hwang, H.-S. Oh, Highly selective and stackable electrode design for gaseous CO<sub>2</sub> electroreduction to ethylene in a zero-gap configuration, *Nano Energy* 84 (2021), 105859, <https://doi.org/10.1016/j.nanoen.2021.105859>.
- [23] W. Liu, P. Zhai, A. Li, B. Wei, K. Si, Y. Wei, X. Wang, G. Zhu, Q. Chen, X. Gu, R. Zhang, W. Zhou, Y. Gong, Electrochemical CO<sub>2</sub> reduction to ethylene by ultrathin CuO nanoplate arrays, *Nat. Commun.* 13 (2022) 1877, <https://doi.org/10.1038/s41467-022-29428-9>.
- [24] J. Wang, H.Y. Tan, Y. Zhu, H. Chu, H.M. Chen, Linking the dynamic chemical state of catalysts with the product profile of electrocatalytic CO<sub>2</sub> reduction, *Angew. Chem.* 133 (2021) 17394–17407, <https://doi.org/10.1002/ange.202017181>.
- [25] F. Yang, W. Fang, Q. Wang, P. Deng, B.Y. Xia, Optimizing copper oxidation state to promote ethylene generation in efficient carbon dioxide conversion, *ACS Sustain. Chem. Eng.* 10 (2022) 4677–4682, <https://doi.org/10.1021/acscuschemeng.2c00123>.
- [26] C.W. Li, M.W. Kanan, CO<sub>2</sub> reduction at low overpotential on Cu electrodes resulting from the reduction of thick Cu<sub>2</sub>O films, *J. Am. Chem. Soc.* 134 (2012) 7231–7234, <https://doi.org/10.1021/ja3010978>.
- [27] Y. Zhou, F. Che, M. Liu, C. Zou, Z. Liang, P. De Luna, H. Yuan, J. Li, Z. Wang, H. Xie, H. Li, P. Chen, E. Bladt, R. Quintero-Bermudez, T.-K. Sham, S. Bals, J. Hofkens, D. Sinton, G. Chen, E.H. Sargent, Dopant-induced electron localization

- drives CO<sub>2</sub> reduction to C<sub>2</sub> hydrocarbons, *Nat. Chem.* 10 (9) (2018) 974–980, <https://doi.org/10.1038/s41557-018-0092-x>.
- [28] C. Chen, X. Sun, L. Lu, D. Yang, J. Ma, Q. Zhu, Q. Qian, B. Han, Efficient electroreduction of CO<sub>2</sub> to C<sub>2</sub> products over B-doped oxide-derived copper, *Green Chem.* 20 (2018) 4579–4583, <https://doi.org/10.1039/C8GC02389A>.
- [29] J. Liu, L. Cheng, Y. Wang, R. Chen, C. Xiao, X. Zhou, Y. Zhu, Y. Li, C. Li, Dynamic determination of Cu<sup>+</sup> roles for CO<sub>2</sub> reduction on electrochemically stable Cu<sub>2</sub>O-based nanocubes, *J. Mater. Chem. A* 10 (2022) 8459–8465, <https://doi.org/10.1039/D1TA10831J>.
- [30] Z.-Q. Liang, T.-T. Zhuang, A. Seifitokaldani, J. Li, C.-W. Huang, C.-S. Tan, Y. Li, P. De Luna, C.T. Dinh, Y. Hu, Q. Xiao, P.-L. Hsieh, Y. Wang, F. Li, R. Quintero-Bermudez, Y. Zhou, P. Chen, Y. Pang, S.-C. Lo, L.-J. Chen, H. Tan, Z. Xu, S. Zhao, D. Sinton, E.H. Sargent, Copper-on-nitride enhances the stable electrosynthesis of multi-carbon products from CO<sub>2</sub>, *Nat. Commun.* 9 (2018) 3828, <https://doi.org/10.1038/s41467-018-06311-0>.
- [31] P.-P. Yang, X.-L. Zhang, F.-Y. Gao, Y.-R. Zheng, Z.-Z. Niu, X. Yu, R. Liu, Z.-Z. Wu, S. Qin, L.-P. Chi, Y. Duan, T. Ma, X.-S. Zheng, J.-F. Zhu, H.-J. Wang, M.-R. Gao, S.-H. Yu, Protecting copper oxidation state via intermediate confinement for selective CO<sub>2</sub> electroreduction to C<sub>2+</sub> fuels, *J. Am. Chem. Soc.* 142 (2020) 6400–6408, <https://doi.org/10.1021/jacs.0c01699>.
- [32] X. Yuan, S. Chen, D. Cheng, L. Li, W. Zhu, D. Zhong, Z.-J. Zhao, J. Li, T. Wang, J. Gong, Controllable Cu<sup>0</sup>-Cu<sup>+</sup> sites for electrocatalytic reduction of carbon dioxide, *Angew. Chem.* 133 (2021) 15472–15475, <https://doi.org/10.1002/ange.202105118>.
- [33] T.C. Chou, C.C. Chang, H.L. Yu, W.Y. Yu, C.L. Dong, J.J. Velasco-Velez, C. H. Chuang, L.C. Chen, J.F. Lee, J.M. Chen, H.L. Wu, Controlling the oxidation state of the Cu electrode and reaction intermediates for electrochemical CO<sub>2</sub> reduction to ethylene, *J. Am. Chem. Soc.* 142 (2020) 2857–2867, <https://doi.org/10.1021/jacs.9b11126>.
- [34] J. Zhu, Y. Su, F. Cheng, J. Chen, Improving the performance of PtRu/C catalysts for methanol oxidation by sensitization and activation treatment, *J. Power Sources* 166 (2007) 331–336, <https://doi.org/10.1016/j.jpowsour.2007.01.087>.
- [35] S.H. Ahn, I. Choi, O.J. Kwon, T. Lim, J.J. Kim, Electrochemical preparation of Pt-based catalysts on carbon paper treated with Sn sensitization and Pd activation, *Int. J. Hydrog. Energy* 37 (2012) 41–50, <https://doi.org/10.1016/j.ijhydene.2011.09.074>.
- [36] C.H. Lee, S.H. Cha, A.R. Kim, J.H. Hong, J.J. Kim, Optimization of a pretreatment for copper electroless deposition on Ta substrates, *J. Electrochem. Soc.* 154 (2007) D182, <https://doi.org/10.1149/1.2432074>.
- [37] N. Fredj, T.D. Burleigh, Transpassive dissolution of copper and rapid formation of brilliant colored copper oxide films, *J. Electrochem. Soc.* 158 (2011) C104, <https://doi.org/10.1149/1.3551525>.
- [38] W. Zhang, C. Huang, Q. Xiao, L. Yu, L. Shuai, P. An, Y. Yu, Atypical oxygen-bearing copper boosts ethylene selectivity toward electrocatalytic CO<sub>2</sub> reduction, *J. Am. Chem. Soc.* 142 (2020) 11417–11427, <https://doi.org/10.1021/jacs.0c01562>.
- [39] S. Anantharaj, H. Sugime, S. Noda, Ultrafast growth of a Cu(OH)<sub>2</sub>-CuO nanoneedle array on Cu foil for methanol oxidation electrocatalysis, *ACS Appl. Mater. Interfaces* 12 (2020) 27327–27338, <https://doi.org/10.1021/acsami.0c08979>.
- [40] S. Anantharaj, H. Sugime, S. Yamaoka, S. Noda, Pushing the limits of rapid anodic growth of CuO/Cu(OH)<sub>2</sub> nanoneedles on Cu for the methanol oxidation reaction: anodization pH is the game changer, *ACS Appl. Energy Mater.* 4 (2021) 899–912, <https://doi.org/10.1021/acsaem.0c02822>.
- [41] M. Qiu, N. Wang, Z. Cui, J. Liu, L. Hou, J. Liu, R. Hu, H. Zhang, Y. Zhao, Evolution of Copper oxide nanoneedle mesh with subtle regulated lyophobicity for high efficiency liquid separation, *J. Mater. Chem. A* 6 (2018) 817–822, <https://doi.org/10.1039/C7TA09217B>.
- [42] A.I. Inamdar, H.S. Chavan, A.T. Aqueel Ahmed, Y. Jo, S. Cho, J. Kim, S.M. Pawar, H. Kim, H. Im, Macroporous Cu(OH)<sub>2</sub> nanorod network fabricated directly on Cu foil as binder-free Lithium-ion battery anode with ultrahigh capacity, *J. Alloy. Compd.* 829 (2020), 154593, <https://doi.org/10.1016/j.jallcom.2020.154593>.
- [43] H.K. Ayask, J.V. Khaki, M.H. Sabzevar, Facile synthesis of copper oxide nanoparticles using copper hydroxide by mechanochemical process, *J. Ultrafine Grained Nanostruct. Mater.* (2015) 37–44, <https://doi.org/10.7508/JUFGNSM.2015.01.006>.
- [44] C.A. Obasanjo, A.S. Zeraati, H.S. Shiran, T.N. Nguyen, S.M. Sadaf, M.G. Kibria, C. T. Dinh, In situ regeneration of copper catalysts for long-term electrochemical CO<sub>2</sub> reduction to multiple carbon products, *J. Mater. Chem. A* 10 (2022) 20059–20070, <https://doi.org/10.1039/D2TA02709G>.
- [45] J. Zhang, Y. Wang, Z. Li, S. Xia, R. Cai, L. Ma, T. Zhang, J. Ackley, S. Yang, Y. Wu, Grain boundary-derived Cu<sup>+</sup>/Cu<sup>0</sup> interfaces in CuO nanosheets for low overpotential carbon dioxide electroreduction to ethylene, *Adv. Sci.* (2022), 2200454, <https://doi.org/10.1002/advs.202200454>.
- [46] Q.T. Trinh, K. Bholra, P.N. Amaniampong, F. Jérôme, S.H. Mushrif, Synergistic application of XPS and DFT to investigate metal oxide surface catalysis, *J. Phys. Chem. C* 122 (2018) 22397–22406, <https://doi.org/10.1021/acs.jpcc.8b05499>.
- [47] X. Deng, T. Herranz, C. Weis, H. Bluhm, M. Salmeron, Adsorption of water on Cu<sub>2</sub>O and Al<sub>2</sub>O<sub>3</sub> thin films, *J. Phys. Chem. C* 112 (2008) 9668–9672, <https://doi.org/10.1021/jp800944r>.
- [48] Z.-J. Zuo, J. Li, P.-D. Han, W. Huang, XPS and DFT studies on the autoxidation process of Cu sheet at room temperature, *J. Phys. Chem. C* 118 (2014) 20332–20345, <https://doi.org/10.1021/jp504977p>.
- [49] S.K. Chawla, N. Sankarraman, N. Payer, Diagnostic spectra for XPS analysis of Cu-O-S-H compounds, *J. Electron Spectrosc. Relat. Phenom.* 61 (1992) 1–18, [https://doi.org/10.1016/0368-2048\(92\)80047-C](https://doi.org/10.1016/0368-2048(92)80047-C).
- [50] S. Poulston, P.M. Parlett, P. Stone, M. Bowker, Surface oxidation and reduction of CuO and Cu<sub>2</sub>O studied using XPS and XAES, *Surf. Interface Anal.* 24 (1996) 811–820, [https://doi.org/10.1002/\(SICI\)1096-9918\(199611\)24:12<811::AID-SIA191>3.0.CO;2-Z](https://doi.org/10.1002/(SICI)1096-9918(199611)24:12<811::AID-SIA191>3.0.CO;2-Z).
- [51] L. Schlur, K. Bonnot, D. Spitzer, Synthesis of Cu (OH)<sub>2</sub> and CuO nanotubes arrays on a silicon wafer, *RSC Adv.* 5 (2015) 6061–6070, <https://doi.org/10.1039/C4RA10155C>.
- [52] L. Schlur, P. Agostini, G. Thomas, G. Gerer, J. Grau, D. Spitzer, Detection of organophosphorous chemical agents with CuO-nanorod-modified microcantilevers, *Sensors* 20 (2020) 1061, <https://doi.org/10.3390/s20041061>.
- [53] F. Yang, P. Song, X. Liu, B. Mei, W. Xing, Z. Jiang, L. Gu, W. Xu, Highly efficient CO<sub>2</sub> electroreduction on ZnN<sub>4</sub>-based single-atom catalyst, *Angew. Chem. Int. Ed.* 130 (2018) 12483–12487, <https://doi.org/10.1002/anie.201805871>.
- [54] X. Zhang, Z. Zhang, H. Li, R. Gao, M. Xiao, J. Zhu, M. Feng, Z. Chen, Insight into heterogeneous electrocatalyst design understanding for the reduction of carbon dioxide, *Adv. Energy Mater.* 12 (2022), 2201461, <https://doi.org/10.1016/j.jiec.2022.12.030>.
- [55] J. Kim, W. Guo, H. Kim, S. Choe, S.Y. Kim, S.H. Ahn, Gaseous CO<sub>2</sub> electrolysis: progress, challenges, and prospects, *ACS Sustain. Chem. Eng.* 10 (2022) 14092–14111, <https://doi.org/10.1021/acscuschemeng.2c04501>.